published by Ural Federal University
eISSN 2411-1414
chimicatechnoacta.ru

ARTICLE
2023, vol. 10(4), No.202310411
DOI: 10.15826/chimtech.2023.10.4.11

Comparative characteristics of Bi- and La- doped (Ca/Sr)MoO$_4$-based materials with a defect scheelite-type structure

Zoya A. Mikhaylovskaya [a], Alexandra V. Klimova [b] *, Sofia A. Petrova [c], Elizaveta A. Pankrushina [a], Elena S. Buyanova [b]

a: Zavaritsky Institute of Geology and Geochemistry, Ural Branch of the Russian Academy of Sciences, Ekaterinburg 620110, Russia
b: Institute of Natural Sciences and Mathematics, Ural Federal University, Ekaterinburg 620026, Russia
c: Institute of Metallurgy, Ural Branch of the Russian Academy of Sciences, Ekaterinburg 620016, Russia
* Corresponding author: a.v.klimova@urfu.ru

This paper belongs to a Regular Issue.

Abstract

$CaMoO_4$- and $SrMoO_4$-based scheelite-type phases are noteworthy functional materials, whose properties strongly correlate with their structure. This work is devoted to La- or Bi-doped scheelite-type molybdates. The purpose of the present study is to quantify the effect of isolated electron pairs of bismuth on the distortion of the structure and related properties. Conventional solid-state technology was used for the synthesis of $(Ca/Sr)_{1-3x}La_{2x}\Phi_xMoO_4$ and $Sr_{1-3x}Bi_{2x}\Phi_xMoO_4$, ($0.025 \le x \le 0.275$). The structure was investigated by X-ray powder diffraction and Raman spectroscopy. Rates of structure distortion were characterised by the analysis of the autocorrelation function (AAF) of Raman spectra. Energy gaps were calculated by the Kubelka-Munk method. The conductivity was studied with a.c. impedance spectroscopy. For $(Ca/Sr)_{1-3x}(Bi/La)_{2x}\Phi_xMoO_4$ series $0.025 \le x \le 0.15$ compositions show a basic defect scheelite structure, while $0.15 < x \le 0.225$ compositions of Bi-doped samples exhibit tetragonal supercells. The chemical compression of unit cell is more evident in the case of Bi-doping, indicating the preferred orientation of the isolated electron pairs. The distortion of MoO_4 polyhedra showed by AAF was more significant for $Sr_{1-3x}Bi_{2x}\Phi_xMoO_4$ than for $Sr_{1-3x}La_{2x}\Phi_xMoO_4$, the Δcorr parameters for Bi-doped compositions were almost double in comparison with La-doped one in the range of 50–600 cm^{-1} of the Raman shift. The «critical» $x = 0.15$ point was also clearly indicated by Δcorr parameter. The AAF of the Raman spectra of solid oxides was shown to be a good tool for prediction of properties and points of phase transitions in solid oxides.

Keywords

strontium bismuth molybdate
calcium bismuth molybdate
X-ray diffraction
Raman spectroscopy
autocorrelation function
conductivity
energy gap

Received: 20.10.23
Revised: 17.11.23
Accepted: 27.11.23
Available online: 06.12.23

Key findings

- The AAF demonstrated that the isolated electron pair of bismuth plays a key role in the distortion of the Mo–O sublattice.
- The decrease in the calculated energy gap with increasing *x*-value is observed both for the $(Ca/Sr)_{1-3x}La_{2x}\Phi_xMoO_4$ and $Sr_{1-3x}Bi_{2x}\Phi_xMoO_4$ systems.
- In contrast to $Sr_{1-3x}Bi_{2x}\Phi_xMoO_4$ compositions, $(Ca/Sr)_{1-3x}La_{2x}\Phi_xMoO_4$ show the general decrease of conductivity.

1. Introduction

In recent years, $CaMoO_4$-based and $SrMoO_4$-based phases have attracted interest in many technological fields because of a broad range of applications. For example, such materials can be used in catalytic systems, such as photocatalysts and pigments [1, 2], ionic conductors, microwave devices [3, 4–7], photoluminescent devices [3, 8–10], etc. [1–10]. Usually $CaMoO_4$ and $SrMoO_4$-based phases show scheelite-type structure, and properties of these complex oxides are strongly correlated with the nature and concentration of dopants [3, 7–10].

One of the most popular ways of modifying the properties of the (Ca/Sr)MoO_4 systems is A site doping by trivalent Me^{3+} cations [3, 4, 7–9, 11, 12]. It can be realised in following ways:

1) formation of ($A_{1-x}M_xBO_{4+x/2}$) solid solutions as in works [8, 12, 13];

2) co-substitution in A or B sites by subvalent cations forming $A_{1-2x}Me^{3+}{}_xMe^{+}{}_xBO_4$ or $A_{1-x}Me^{3+}{}_xB_{1-x}Me^{5+}{}_xO_4$ solid solutions, respectively [7];

3) formation of cation vacancies ($A_{1-3x}M_{2x}\Phi_xBO_4$) [11, 12].

In the present work the third way was used. We studied (Ca/Sr)$_{1-3x}La_{2x}\Phi_xMoO_4$ solid solutions in comparison with the (Ca/Sr)$_{1-3x}Bi_{2x}\Phi_xMoO_4$ solid solutions, where Φ is the cation vacancy. The limiting cases of such systems are $CaMoO_4$ or $SrMoO_4$ with an ideal scheelite structure and (La/Bi)$_{2/3}MoO_4$ with a highly distorted scheelite structure [14]. $Ca_{1-3x}Bi_{2x}\Phi_xMoO_4$ and $Sr_{1-3x}Bi_{2x}\Phi_xMoO_4$ were investigated in the previous works [11, 15–17]. The (Ca/Sr)$_{1-3x}Bi_{2x}\Phi_xMoO_4$ compounds were first described by Sleight and Aykan [15] for the x = 0.04 compositions in the (Ca/Sr)$_{1-3x}Bi_{2x}\Phi_xMoO_4$ systems. They exhibit the tetragonal scheelite structure. Guo et al. [11, 16] synthesized compositions in the $Ca_{1-3x}Bi_{2x}\Phi_xMoO_4$ system in the range $0.005 \le x \le 0.20$ and examined their microstructures and microwave dielectric properties. The $0.00 \le x \le 0.15$ compositions were single-phase and had the tetragonal scheelite structure with cationic vacancies. The $x = 0.2$ composition was reported to contain a second unidentified phase. Vibrational spectroscopy results revealed large distortions of MoO_4 and BiO_8 polyhedra [11] with a strong correlation between the A site substitution and the microwave dielectric properties. In later works, additional peaks identified by Guo et al. in the compositions of $Ca_{1-3x}Bi_{2x}\Phi_xMoO_4$ above $x = 0.15$ could be indexed in the tetragonal supercell with $a_{sup} \approx \sqrt{5}a$, $c_{sup} \approx c$ (where a and c are the tetragonal scheelite cell parameters) [16–18]. This superstructure was evident throughout the compositional range $0.15 < x \le 0.225$ and was caused by bismuth ions ordering. The electrical conductivity and the photocatalytic activity of $Ca_{1-3x}Bi_{2x}\Phi_xMoO_4$ were found to be higher in the samples with higher Bi content [17]. In contrast, the electrical conductivity and photocatalytic activity of $Sr_{1-3x}Bi_{2x}\Phi_xMoO_4$ has not been reported yet, and there are no vibrational spectroscopy data for such compounds.

$La_{2/3}MoO_4$ ($La_2Mo_3O_{12}$) and $Bi_{2/3}MoO_4$ ($Bi_2Mo_3O_{12}$) were also reported as conductors [19, 20] and luminescent materials [21]. $La_{2/3}MoO_4$ and $Bi_{2/3}MoO_4$ molybdates represent different structural variants that exist in the defect scheelite. Both structure types are characterized by a unique ordering of the trivalent cations and cation vacancies [22]. $Bi_{2/3}MoO_4$ (space group P2₁/c) contains three scheelite subcells per unit cell, which include tetrahedral pairs of [Mo_2O_8] groups [23]. This specific ordering is driven by the asymmetric nature of the Bi^{3+} cation with its directionally oriented lone pair of electrons, resulting from similar ionic radii of Bi^{3+} and La^{3+} [22]. In contrast to Bi^{3+}, the asymmetry for La^{3+} cations is absent from the $La_{2/3}MoO_4$ (space group C2/c). Therefore, in the case of (Ca/Sr)$_{1-3x}$(Bi/La)$_{2x}\Phi_xMoO_4$ solid solutions the lone electron pair effect of Bi^{3+} is expected to impact the structure and properties of these compounds [22].

Here we present a study of the (Ca/Sr)$_{1-3x}La_{2x}\Phi_xMoO_4$ system in comparison with $Sr_{1-3x}Bi_{2x}\Phi_xMoO_4$ system, which also might be expected to be a promising ionic conductor, catalyst, dialectic material, etc. The structural features were examined using X-ray diffraction and Raman spectroscopy. The autocorrelation function analysis was used to examine trends in similar samples of Bi- and La-doped strontium molybdates. The decreasing trend in the energy gap values calculated using the Kubelka-Munk method and UV-Vis spectroscopy was shown. The conductive properties of doped strontium molybdates were examined by impedance spectroscopy.

2. Experimental

Compositions of the general formula (Ca/Sr)$_{1-3x}La_{2x}\Phi_xMoO_4$ and $Sr_{1-3x}Bi_{2x}\Phi_xMoO_4$, ($0.025 \le x \le 0.275$) series were synthesized by a conventional solid state method [18] from $SrCO_3$ (99.0%, Reakhim), Bi_2O_3 (99.9%, Merck), La_2O_3 (99.9%, Merck) and MoO_3 (99.5%, Reakhim) in the range of 600–900 °C and 500–700 °C respectively. The density of the homogeneous powders (ρ_{exp}) was determined using 2 ml pycnometers with distilled water as the displacement liquid.

X-ray powder diffraction data were obtained using a Bruker Advance D8 diffractometer with a VANTEC1 detector (Ni filtered Cu Kα radiation, θ/θ geometry) in Ural-M center of Institute of Metallurgy. The data were collected in the 2θ range of 6–120°, in steps of 0.02103° with an effective scan time of 200 s per step.

Raman spectra were obtained for Sr_{1-3x}(Bi/La)$_{2x}\Phi_xMoO_4$ series with a Horiba LabRam HR800 Evolution spectrometer equipped with an Olympus BX-FM confocal microscope (50× objective, numerical aperture = 0.7) and He-Ne laser (radiation wavelength 633 nm) and 600 gr/mm grating. The spectral resolution was about 1 cm^{-1}, and the spatial lateral resolution was about 2 μm. The spectra were fitted using a Gaussian-Lorentzian model. The UV-Vis spectra were obtained in the range 350–1100 nm using a Thermo Scientific Evolution 300 spectrophotometer equipped with an integrating sphere. Energy gaps for direct inter-band transitions were calculated by linear approximation of the Kubelka-Munk function [24]. The a.c. impedance spectra were obtained with an Elins Z-3000 impedancemeter for ceramic samples of (Ca/Sr)$_{1-3x}La_{2x}\Phi_xMoO_4$ and $Sr_{1-3x}Bi_{2x}\Phi_xMoO_4$ with platinum electrodes.

3. Results and Discussions

Figure 1 shows the X-ray diffraction patterns of representative compositions in the $Ca_{1-3x}La_{2x}\Phi_xMoO_4$ and $Sr_{1-3x}La_{2x}\Phi_xMoO_4$ systems. In the compositional range $0 \le x \le 0.15$, the patterns of (Ca/Sr)$_{1-3x}La_{2x}\Phi_xMoO_4$ can be indexed using a tetragonal scheelite model in the space group I4₁/a with no additional reflections.

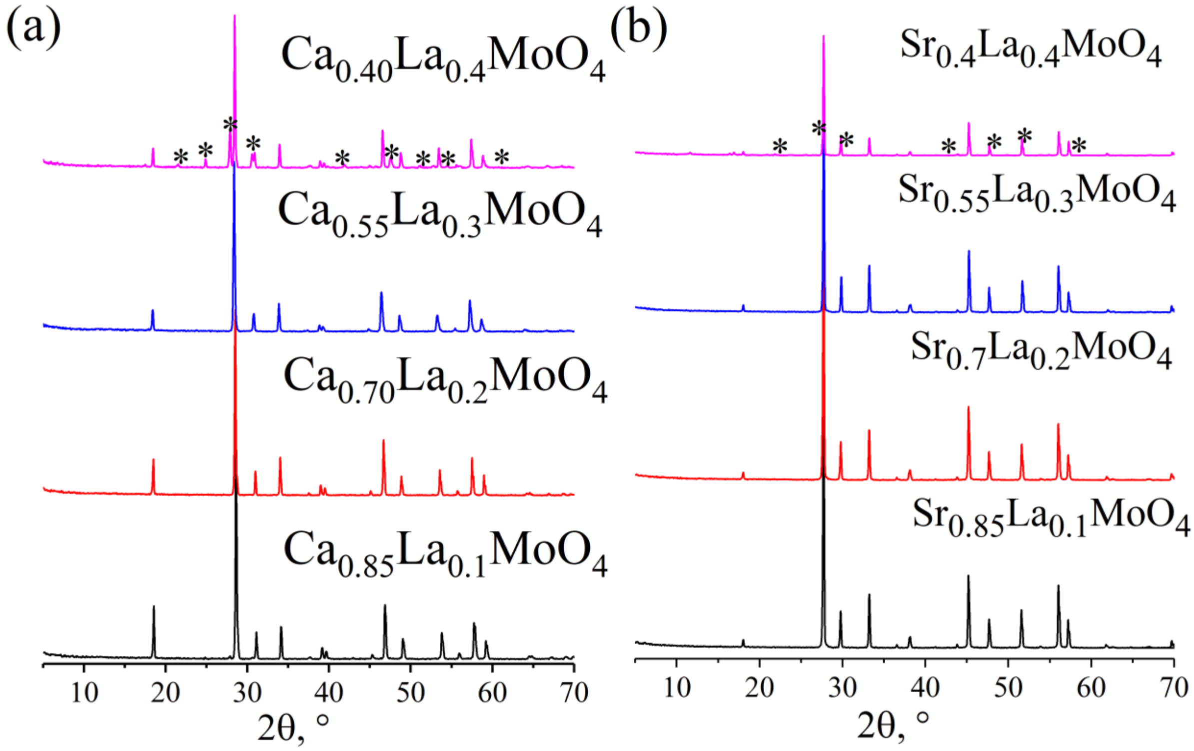

Figure 1 Detail of X-ray diffraction patterns of selected compositions of the $(Ca/Sr)_{1-3x}La_{2x}\Phi_xMoO_4$ systems. Peaks of $La_2Mo_3O_{12}$ are marked with asterisks.

XPRD patterns of $x \geq 0.2$ compositions contain reflections of $(Ca/Sr)MoO_4$ and $La_2Mo_3O_{12}$ phases. In the $Sr_{1-3x}Bi_{2x}\Phi_xMoO_4$ system ($0 \leq x \leq 0.125$), the patterns were indexed using a tetragonal scheelite model, while the patterns for the ($0.125 \leq x \leq 0.225$) compositions were indexed using a superstructured scheelite model ($a_{sup} = \sqrt{5}a_{sub}$, $c_{sup} = c_{sub}$), as in the previous studies [17, 18].

The compositional dependence of the unit cell parameters is shown in Figure 2. A general decrease in the unit cell parameters is observed over the compositional range studied, which is attributable to the substitution of Sr^{2+} by smaller Bi^{3+} and La^{3+}cations with ionic radii of 1.26, 1.17 Å and 1.16 Å, respectively [25]. The opposite correlation is observed for Ca^{2+} replaced with Bi^{3+} and La^{3+}cations: due to its smaller ionic radius of 1.12 Å [25] the unit cell parameters generally increase. Two linear ranges for both basic and superstructured complex oxides are observed for the Bi-doped compositions. For $Ca_{1-3x}La_{2x}\Phi_xMoO_4$ and $Sr_{1-3x}La_{2x}\Phi_xMoO_4$ no additional ordering was observed, and there is only one linear range on the graphs. The chemical compression of the unit cell of bismuth-substituted $SrMoO_4$ is more significant than that in the case of doping by lanthanum. This indicates that the average ionic radii of bismuth can be less than 1.17 Å, probably due to the preferred orientation of $6s^2$ electronic pair of bismuth. The measured densities are in good agreement with the theoretical values calculated from the X-ray data (within 2%). Bi-doped samples showed the most intensive growth of density with x.

Changes of structure of Bi- and La-doped strontium molybdates were investigated with Raman spectroscopy. The general compression of unit cell of $Sr_{1-3x}(Bi/La)_{2x}\Phi_xMoO_4$ results in more evident distortion of the structure fragments, whereas the general expansion of $Ca_{1-3x}La_{2x}\Phi_xMoO_4$ can result in a minimisation of the distortion. The recorded Raman spectra are shown in Figure 3. The lattice vibrations in the scheelite-structured compounds include internal modes that correspond to vibrations inside the $[MoO_4]^{2-}$ tetrahedra and external modes that are assigned to lattice vibrations. Because of crystal field effects and Davydov splitting, the degeneracy of the $[MoO_4]^{2-}$ vibrations corresponding to Td symmetry in free space is resolved.

The group theoretical analysis predicts that 26 modes are possible in the case of tetragonal scheelite-structured compounds in space group $I4_1/a$, which are distributed as irreducible representations [26–28]: $\Gamma = 3A_g + 5B_g + 5E_g + 5A_u + 3B_u + 5E_u$, of which the A_g, B_g and E_g vibrations are Raman active, whereas the A_u, B_u and E_u vibrations are infrared active. In the present study, 13 vibrational modes are observed for the end member $SrMoO_4$, which is in good agreement with previous experimental and calculated results for this composition [26–28]. According to the previous studies, the modes in the low-frequency range of spectra (modes 1–6 in Figure 3) correspond to the external modes of O–Mo–O and O–Sr–O bands [29–31], while medium and high frequency ranges contain internal vibrations (modes 7–13 in Figure 3). The Mo–O bending modes are found to be located at medium frequencies (ν_2 and ν_4, modes 7–10) while the Mo–O stretching modes are detected at high frequencies (ν_1 and ν_3, modes 11–13) [27–29, 11].

Doping of strontium molybdates with Bi^{3+} and La^{3+} leads to a broadening of peaks in the Raman spectrum and the appearance of additional modes.

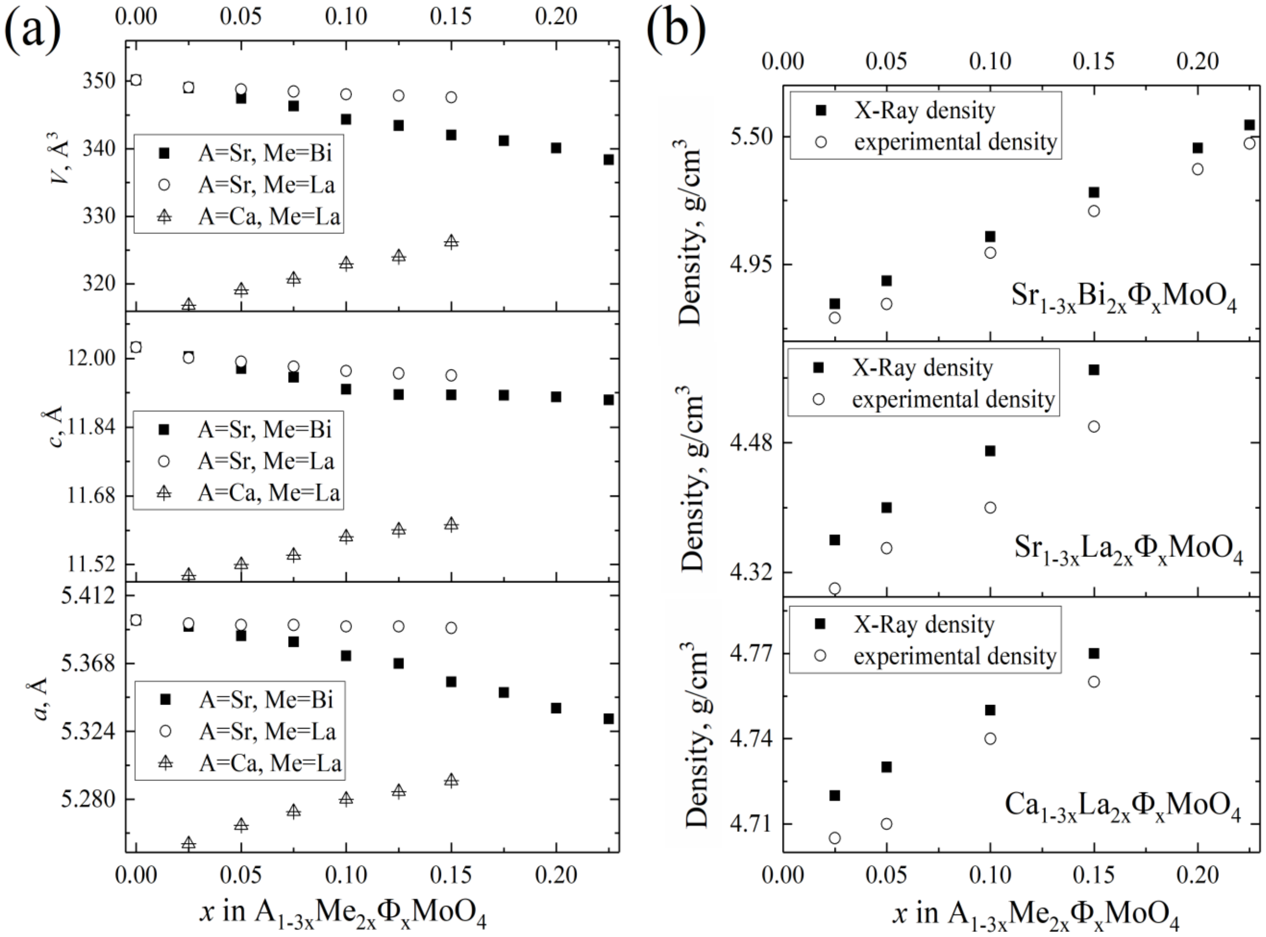

Figure 2 Unit cell parameters, unit cell volume (a), calculated and measured densities (b) of (Ca/Sr)$_{1-3x}$La$_{2x}\mathit{\Phi}_x$MoO$_4$ and Sr$_{1-3x}$Bi$_{2x}\mathit{\Phi}_x$MoO$_4$ compositions. For x=0.15...0.225 compositions of Sr$_{1-3x}$Bi$_{2x}\mathit{\Phi}_x$MoO$_4$ series subcell values are shown (a'=a/√5, V' = V/5).

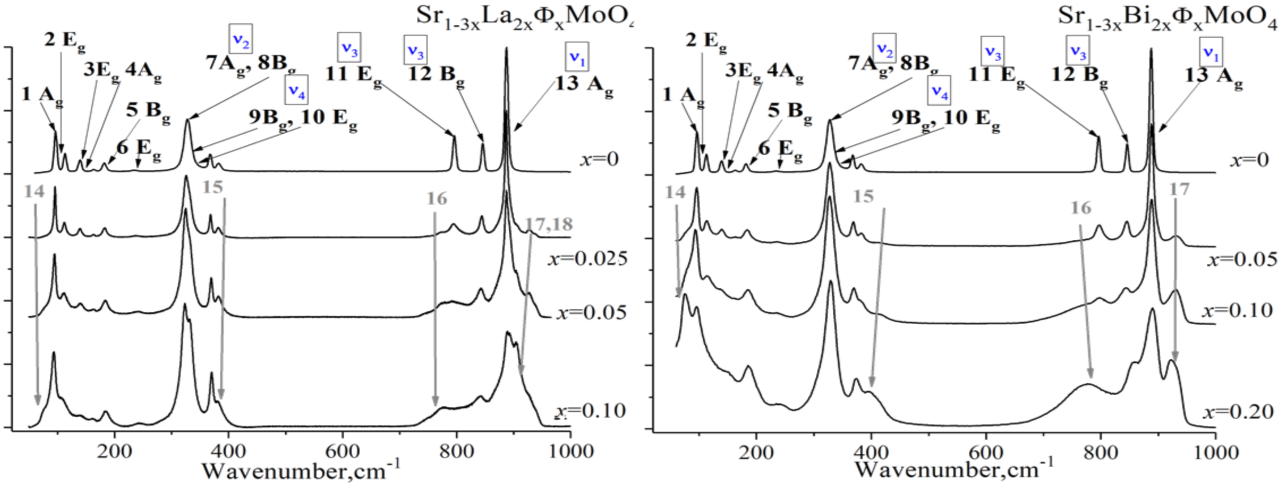

Figure 3 Raman spectra of selected compositions in the Sr$_{1-3x}$Bi$_{2x}\mathit{\Phi}_x$MoO$_4$ and Sr$_{1-3x}$La$_{2x}\mathit{\Phi}_x$MoO$_4$ systems. Additional modes are shown in grey color.

The following additional modes were detected: "mode-14" at 80–87 cm^{-1}, "mode-15" at 406–412 cm^{-1}, "mode-16" at 770–790 cm^{-1} and "mode-17 and 18" at 925–932 cm^{-1}. Modes-14-16 are probably associated with distorted MoO$_4$ tetrahedra as it was suggested by Guo et al. [11] in the case of Ca$_{1-3x}$Bi$_{2x}\mathit{\Phi}_x$MoO$_4$ system. The modes-17 and 18 have been previously detected for SrMoO$_4$ at high pressure (12 GPa) [30], where SrMoO$_4$ had a distorted scheelite structure, and these modes were also associated with ν$_1$ Mo–O stretching vibrations. In this work chemical compression of the unit cell can result a similar distortion of MoO$_4$ polyhedra. Hence "mode-17" and "mode-18" can be also ascribed to a short Mo–O bondvibration.

Unfortunately, the compositional variations of these modes and the full width at half maximum (FWHM) are not absolutely clear because of significant broadening of the peaks.

Figure 4 shows the examples of peak fitting for several compositions, indicating a high overlap of spectral lines.

DOI: 10.15826/chimtech.2023.10.4.11

We can only point out the general increasing trend of FWHM values with increasing *x*-value. This indicates a variation in the length of Mo–O bonds, but a correct direct quantitative analysis is impossible. That is why we used an analysis of autocorrelation function (AAF). Salje et al. [31] proposed an autocorrelation function Corr(α,ω') as a way of parametrizing effective line widths in IR spectra in order to examine trends in similar samples. The AAF method was later adapted for examining Raman spectra by Pankrushina et al. [32]. Corr(α,ω') can be calculated using Equation 1:

$$\mathrm{Corr}(\alpha,\omega') = \int_{-\infty}^{\infty} \alpha(\omega+\omega')\alpha(\omega)d\omega, \tag{1}$$

where α(ω) is the primary spectrum and α(ω + ω') is a replica of the spectrum shifted by ω'.

Salje et al. [31] calculated the Δcorr parameter as follows: the background was subtracted from the α(ω) initial spectrum, the Corr(α,ω') was calculated and normalised, and then the Corr(α,ω') peak apex is approximated by the Gaussian function. The Δcorr parameter is determined by extrapolating the *σ* function to the Δω' = 0 point using second-order polynomials. In this work a modified Gaussian function [32] was used. Thus, Δcorr is an approximation of the σ parameter of the Gaussian function, which is calculated from the Corr(α,ω'*)* peak apex and is proportional to the full widths at half maximum (FWHM) of the autocorrelation function. At the same time, Δcorr is the average estimate of the FWHM of the peaks in the spectrum. In the present work Δcorr was calculated over three frequency ranges (50–250 $\mathrm{cm^{-1}}$, 250–600 $\mathrm{cm^{-1}}$ and 600–1000 $\mathrm{cm^{-1}}$, covering the lattice modes, $\nu_2 + \nu_4$ and $\nu_1 + \nu_3 + \nu_4$, respectively). For all wavenumber ranges, Δcorr (i.e., FWHM values) increases. This indicates a systematic distortion of $\mathrm{MoO_4}$ polyhedra. However, in the case of $\mathrm{Sr_{1-3\mathit{x}}Bi_{2\mathit{x}}}\mathit{\Phi}_x\mathrm{MoO_4}$ it increases up to *x* = 0.15, and above *x* = 0.15 Δcorr either decreases or changes little. It means that ordering in A-sublattice results the reduction of the distortion of $\mathrm{MoO_4}$ polyhedra. For $\mathrm{Sr_{1-3\mathit{x}}La_{2\mathit{x}}}\mathit{\Phi}_x\mathrm{MoO_4}$ Δcorr also increases but in general the values of Δcorr is smaller. It indicates that $6s^2$ pair of bismuth is a strong factor of the distortion of molybdenum-oxygen sublattice.

Typical optical diffuse scattering spectra and Tauc plots are shown in Figure 6. The scattering in the range of ~500–1100 nm is close to 100%. The spectrum for $\mathrm{SrMoO_4}$ contains a broad band in the range of 200–300 nm, which corresponds to electronic transitions within the molybdate tetrahedra [33]. In the substituted samples, this band slightly shifts to a higher wavelength (Figure 6). In general, the spectra are similar to those of $\mathrm{(Ca/Sr)_{1-3\mathit{x}}Bi_{2\mathit{x}}}\mathit{\Phi}_x\mathrm{MoO_4}$ [18]. Band gap (E_g) calculations were performed using the Kublenka-Munk theory and the Tauc relation [24]. The value of E_g can be obtained by interpolating the linear part of the Tauc plots.

Band gap values decreased with increasing *x*-value (Table 1) for both $\mathrm{Bi^{3+}}$ and $\mathrm{La^{3+}}$ doping. The conduction band (CB) in $\mathrm{SrMoO_4}$ is formed by Mo 4*d* states with some mixing of the O 2*p* states [26, 27], and the Mo 4*d* states in CB are split by the tetrahedral crystal field into two groups of states, as in other scheelite compounds [26, 27, 34].

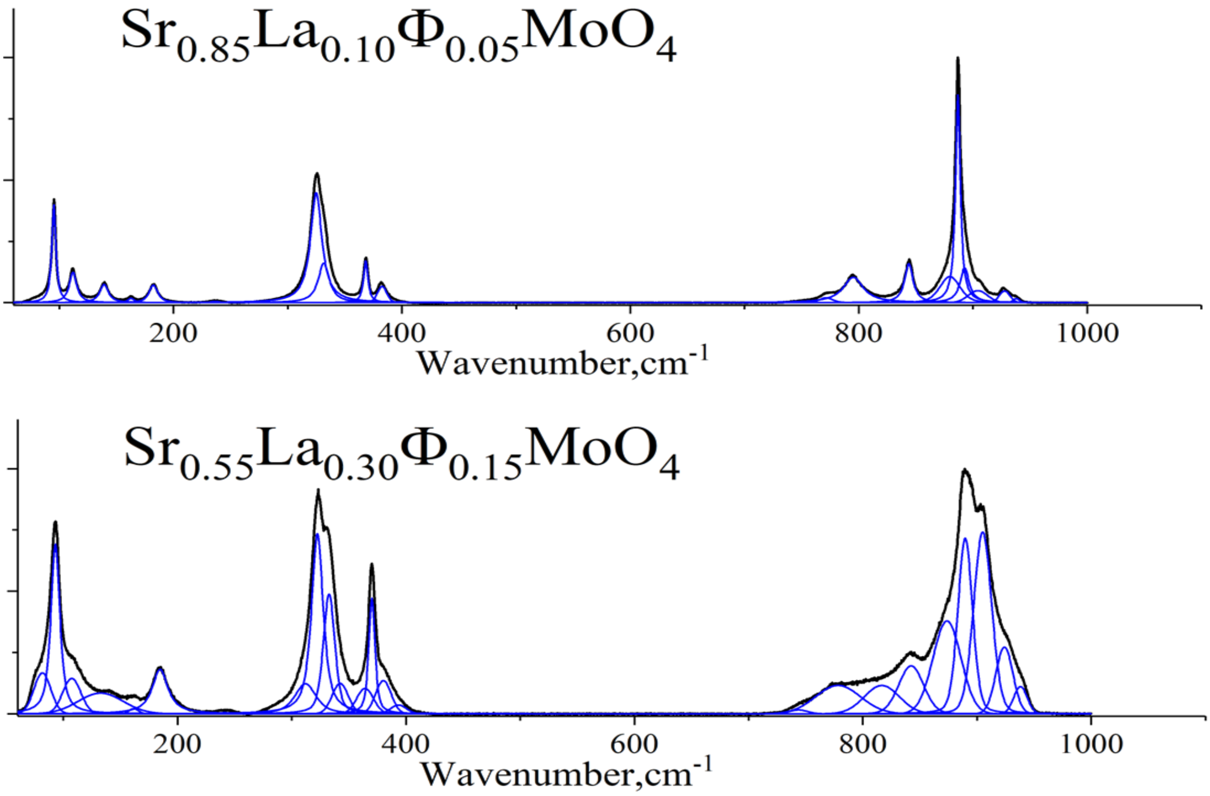

Figure 4 Examples of fitting by Gauss functions are shown for the selected Raman spectra for $\mathrm{Sr_{1-3\mathit{x}}La_{2\mathit{x}}}\mathit{\Phi}_x\mathrm{MoO_4}$.

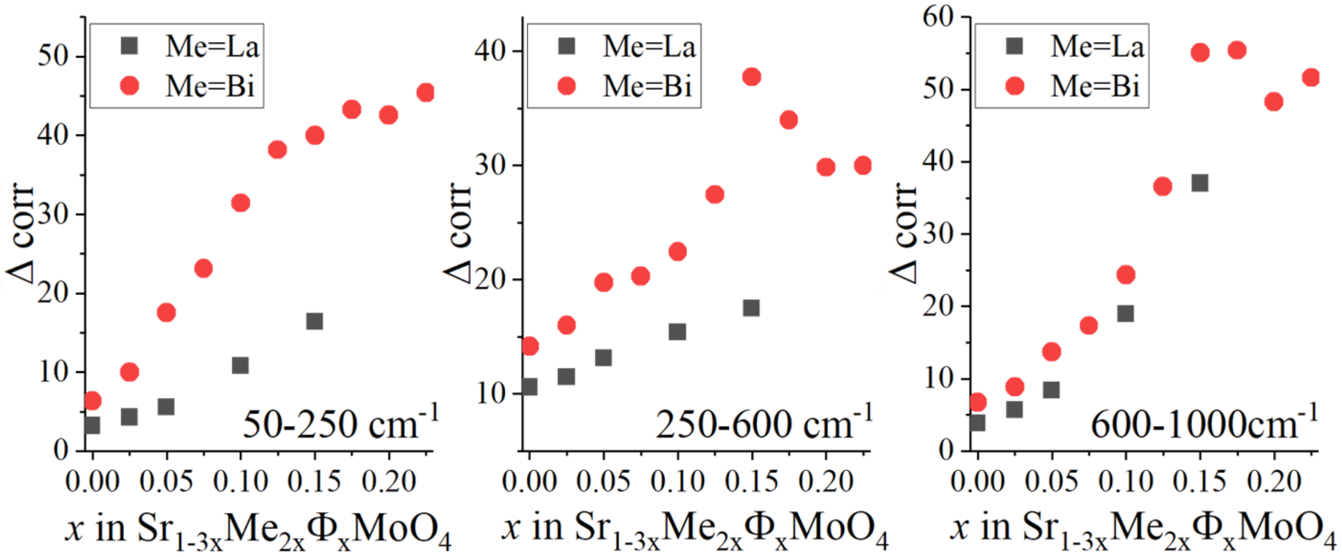

Figure 5 Compositional variation of Δcorr over different frequency ranges.

In the case of doping with Me^{3+}, the splitting of the CB is expected to be absent because of the distortion of the MoO_4 polyhedra. It can also lead to a slight decrease of E_g like in the case of doping by lanthanum (Table 1). In the case of bismuth, the energy gap decreases substantially, probably because of the additional Bi 6*p* states in the electronic spectra [35]. Such a band gap decrease is favourable for the use of Bi-doped molybdates as yellow pigments or as photocatalysts.

The conductivity of $(Ca/Sr)_{1-3x}La_{2x}\Phi_xMoO_4$ and $Sr_{1-3x}Bi_{2x}\Phi_xMoO_4$ was studied by a.c. impedance spectroscopy in the temperature ranges of 400–900 °C and 400–700 °C, respectively. $SrMoO_4$ is known to be an ionic conductor with t_{O2-} close to 1 [36]. The impedance spectra were similar for all compositions over the measurement range, showing semicircles with a zero high frequency intercept on the real axis (Figure 7). The equivalent circuit consists of a parallel combination of a resistor (R) and a capacitor (C), as in the previous work devoted to the molybdates of calcium and strontium [36]. The capacitance value (C) was found to be ~10^{-11} F, corresponding to the total impedance of the electrolyte [37]. Separation of the total resistance into bulk and grain boundary components was not possible.

Arrhenius plots of the total conductivity and compositional variation of conductivity at 873 K for the $Sr_{1-3x}Bi_{2x}\Phi_xMoO_4$ series are presented in Figure 8. The Arrhenius plots are generally linear, with a slight deviation from the linearity caused by kinetic restraints at low temperatures. The conductivity of $SrMoO_4$ is in good agreement with the previous studies [36]. All $Sr_{1-3x}Bi_{2x}\Phi_xMoO_4$ compositions show increased conductivity in comparison to $SrMoO_4$.

The activation energy changes insignificantly (from ~1.2 to ~1.1 eV for $Ca_{1-3x}La_{2x}MoO_4$, from ~0.8 to 0.85 eV for $Ca_{1-3x}Bi_{2x}MoO_4$ and from ~ 1.30 to 1.41 for $Sr_{1-3x}La_{2x}MoO_4$), indicating that the conduction mechanism in doped molybdates in general is similar to that in the parent compounds [16].

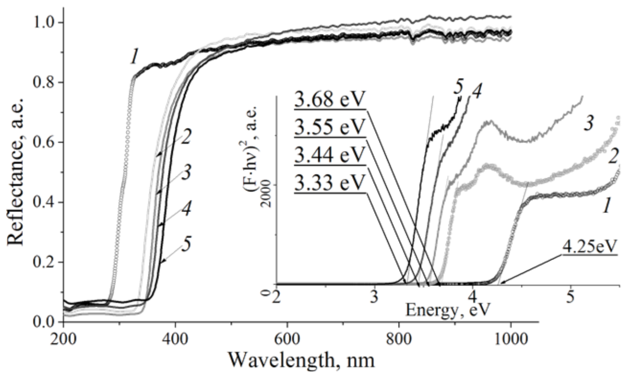

Figure 6 Optical diffuse scattering spectra for selected compositions in the $Sr_{1-3x}Bi_{2x}\Phi_xMoO_4$ system and corresponding Tauc plots (at inset): 1 – $SrMoO_4$; 2 – $x = 0.05$; 3 – $x = 0.10$; 4 – $x = 0.15$; 5 – $x = 0.20$.

Table 1 Compositional variation of optical band gap (E_g direct) in the $A_{1-3x}Me_{2x}\Phi_xMoO_4$, A= Ca/Sr, Me = Bi/La [17, 18].

x	0.05	0.75	0.10	0.125	0.15	0.175	0.2
A = Sr, Me = Bi; E_g, eV	3.68	3.61	3.55	3.48	3.44	3.40	3.33
A = Ca, Me = La; E_g, eV	3.90	3.87	3.84	3.80	3.75	–	–
A = Sr, Me = La; E_g, eV	4.17	4.11	4.08	3.96	3.89	–	–

However, there can be a change in the transference number, with a greater electronic contribution to conductivity. Ionic transport in scheelite-type compounds assumes the presence of irregular interstitial oxygen positions, although these have not been identified using diffraction methods [12]. Therefore, conductivity can be induced by increasing the number of such positions due to the distortion of MoO_4 polyhedra. On the other hand, in scheelite-type compounds additional *n*-type transfer can be realised [38].

DOI: 10.15826/chimtech.2023.10.4.11

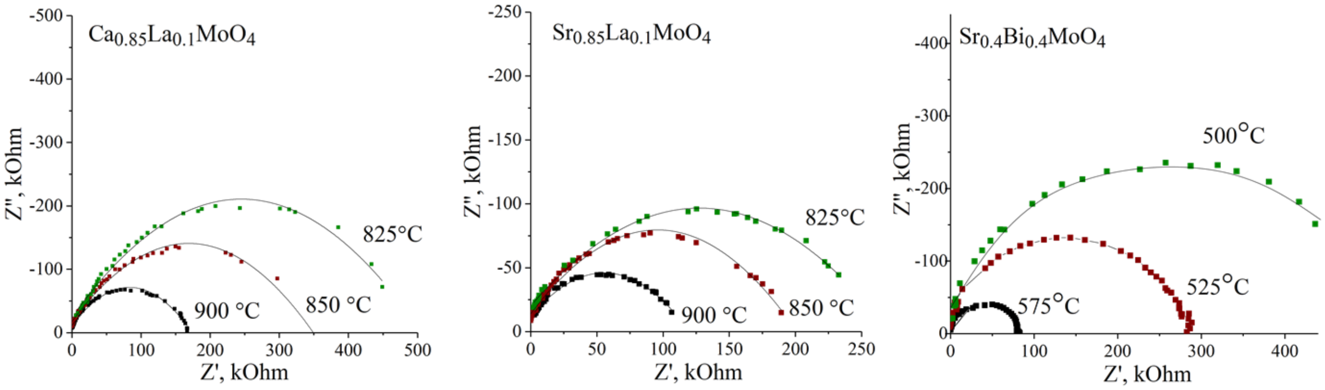

Figure 7 A typical impedance spectrum of $(Ca/Sr)_{1-3x}La_{2x}\Phi_xMoO_4$ and $Sr_{1-3x}Bi_{2x}\Phi_xMoO_4$ systems at different temperatures.

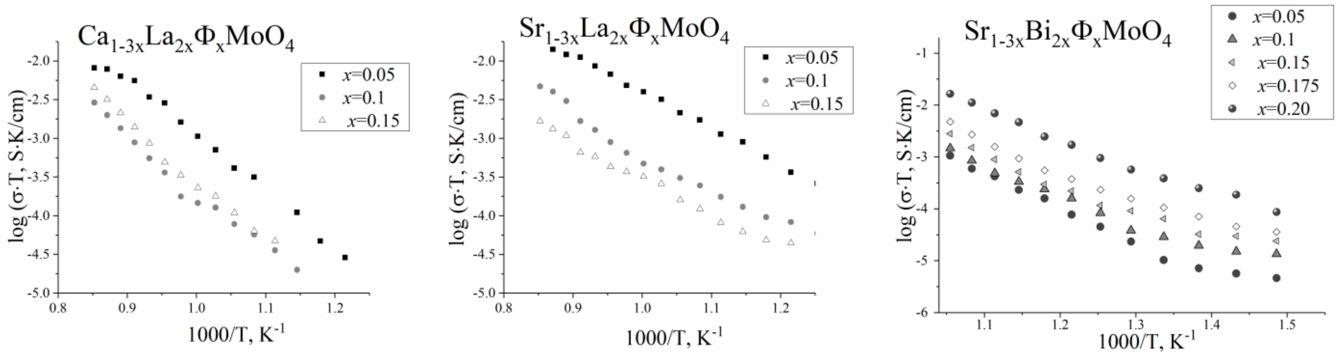

Figure 8 Arrhenius plots of total conductivity for $(Ca/Sr)_{1-3x}La_{2x}\Phi_xMoO_4$ and $Sr_{1-3x}Bi_{2x}\Phi_xMoO_4$ complex oxides.

In the case of $Sr_{1-3x}Bi_{2x}\Phi_xMoO_4$ the *n*-type electronic contribution can be caused by the presence of low concentrations of reduced molybdenum species at the grain surfaces, namely Mo^{4+} and Mo^{5+} ions. The maximum values of total conductivity at 948 K were $1.75\cdot10^{-5}$ S·cm^{-1} and $2.82\cdot10^{-5}$ S·cm^{-1} for the x = 0.200 and x = 0.225 compositions, respectively, which is less than the conductivity of $Bi_2Mo_3O_{12}$ under the same conditions [39]. In contrast to $Sr_{1-3x}Bi_{2x}\Phi_xMoO_4$ compositions $(Ca/Sr)_{1-3x}La_{2x}\Phi_xMoO_4$ show the general decrease of conductivity (Figure 8). Probably, this decrease in conductivity is due to either the smaller distortion of molybdenum-oxygen polyhedra, which causes the decrease of oxygen ion mobility, or the lower concentrations of reduced molybdenum species at the grain surfaces of $(Ca/Sr)_{1-3x}La_{2x}\Phi_xMoO_4$ as compared with $Sr_{1-3x}Bi_{2x}\Phi_xMoO_4$. The maximum values of the total conductivity at 948 K among $(Ca/Sr)_{1-3x}La_{2x}\Phi_xMoO_4$ were $4.34\cdot10^{-7}$ S·cm^{-1} and $2.25\cdot10^{-6}$ S·cm^{-1} for the doped calcium molybdate and strontium molybdate, respectively.

4. Limitations

In this work, the synthesis is highly sensitive to the purity of molybdenum oxide, the insufficient purity of which leads to the formation of non-single-phase samples. Lanthanum oxide should be weighed immediately after annealing at a temperature of at least 1000 °C because lanthanum oxide strongly absorbs H_2O and CO_2.

Bismuth oxide can evaporate during synthesis, which leads to a change in the chemical composition. The chemical composition of compounds can be confirmed by dissolving samples and analyzing them using AES; however, this data were not included in this work. In this study, we were not able to determine the exact oxidation state of molybdenum, so it was taken as Mo^{+6}, since Mo^{+5} is often present in a low concentration on the surface of bismuth molybdates. The maximum frequency measured with the Elins Z-3000 impedancemeter is 1000 kHz. Approximation of spectra by AAF using the Gaussian-Lorentzian model significantly slows down the calculation; therefore, we used the Gaussian model. The diffuse scattering spectra of these complex oxides are very sensitive to sample preparation, e.g. texturing or a small amount of sample leads to large noises.

5. Conclusions

Thus, in the present work, the synthesis of $(Ca/Sr)MoO_4$ doped by La and Bi (what are ions with a close radii) was carried out. A comparative study of their structure and properties was conducted. The results of the investigation of the structure and properties of $(Ca/Sr)_{1-3x}La_{2x}\Phi_xMoO_4$ and $Sr_{1-3x}Bi_{2x}\Phi_xMoO_4$ are consistent with those of the previous studies [11, 16–18]. $Bi^{3+}$and La^{3+}ions possess similar ionic radii; however, the $6s^2$ isolated electron pair of bismuth was shown to be a significant factor in the regulation of structure and properties. A cation vacancy solid solution is formed in the system $Sr_{1-3x}La_{2x}\Phi_xMoO_4$ over the compositional range $0.0 \le x \le 0.15$. Phases of $(Ca/Sr)_{1-3x}La_{2x}\Phi_xMoO_4$ and $Sr_{1-3x}Bi_{2x}\Phi_xMoO_4$ in the range $0.025 \le x \le 0.15$ show a tetragonal scheelite structure, isostructural with $SrMoO_4$, while in the range $0.15 < x \le 0.225$ a tetragonal superstructure is seen for the phases of $Sr_{1-3x}Bi_{2x}\Phi_xMoO_4$. Strong distortion of the MoO_4 polyhedra in $(Ca/Sr)_{1-3x}La_{2x}\Phi_xMoO_4$ and $Sr_{1-3x}Bi_{2x}\Phi_xMoO_4$ was seen in the crystal structure and reflected in the Raman spectra. Using AAF, we demonstrated quantitatively that the isolated electron pair of bismuth plays a key role in the distortion of the Mo–O sublattice. It means that the AAF of the Raman spectra of series of complex oxides can also be used to predict their conductive properties. The Δcorr parameter confirmed the $x = 0.15$ composition to be a "critical" point for $Sr_{1-3x}Bi_{2x}\Phi_xMoO_4$. It indicates a strong change in the structure of $0.15 \leq x \leq 0.225$ compositions caused by bismuth ordering and less distorted MoO_4 polyhedra. The $\Delta corr$ parameter also showed smaller distortion in the case of doping with lanthanum, indicating the significant effect of $6s^2$ isolated electron pair of bismuth. As a result, the conductivity increases with increasing Bi content and decreases with La content. Thus, AAF was shown to be an effective tool to find "critical" points among series of solid solutions.

The decrease of calculated energy gap with increasing x-value is observed both in $(Ca/Sr)_{1-3x}La_{2x}\Phi_xMoO_4$ and $Sr_{1-3x}Bi_{2x}\Phi_xMoO_4$ systems. In the case of bismuth, the energy gap decreases substantially, probably, because of additional the Bi 6p states in electronic spectra. Such a band gap decrease is favorable for using of Bi-doped molybdates as yellow pigments or as photocatalysts. Conductivity increases with increasing x-value in the $Sr_{1-3x}Bi_{2x}\Phi_xMoO_4$ system and decreases in the case of $(Ca/Sr)_{1-3x}La_{2x}\Phi_xMoO_4$ system, also indicating the effect of $6s^2$ isolated electron pair of bismuth. A maximum value of $2.82 \cdot 10^{-5}$ S·cm^{-1} was achieved at 948 K for the $x = 0.255$ composition. The maximum values of the total conductivity among all $(Ca/Sr)_{1-3x}La_{2x}\Phi_xMoO_4$ at 948 K were $4.34 \cdot 10^{-7}$ S·cm^{-1} and $2.25 \cdot 10^{-6}$ S·cm^{-1} for the doped calcium molybdate and strontium molybdate, respectively.

• Supplementary materials

No supplementary materials are available.

• Funding

This work was fulfilled as part of the Government task to the Institute of Geology and Geochemistry (theme No. AAAA-A19-119071090011-6). The retrofit and development of the Geoanalitik Shared Facilities Center of the Institute of Geology and Geochemistry is carried out under a grant from the Ministry of Higher Education and Science of the Russian Federation (agreement No. 075-15-2021-680).

• Acknowledgments

The XRD data were obtained in Ural-M center of Institute for Metallurgy, Ural Branch of RAS, the Raman data were obtained in Geoanalytic center of Zavaritsky Institute of Geology and Geochemistry, Ural Branch of RAS.

• Author contributions

Conceptualization: Z.A.M., E.S.B.
Data curation: Z.A.M., E.S.B., E.A.P.
Formal Analysis: E.S.B., Z.A.M.
Funding acquisition: Z.A.M.
Investigation: Z.A.M., A.V.K., S.A.P., E.A.P.,
Methodology: Z.A.M., E.A.P., S.A.P.
Project administration: Z.A.M.
Resources: E.S.B.
Software: E.S.B., E.A.P.
Supervision: Z.A.M.
Validation: E.S.B.
Visualization: Z.A.M., E.S.B.
Writing – original draft: Z.A.M.
Writing – review & editing: Z.A.M., E.S.B., A.V.K.

• Conflict of interest

The authors declare no conflict of interest.

• Additional information

Author IDs:
Zoya A. Mikhaylovskaya, Scopus ID 26536460700;
Alexandra V. Klimova, Scopus ID 57223927579;
Sofia A. Petrova, Scopus ID 7006291101;
Elizaveta A. Pankrushina, Scopus ID 57204032915;
Elena S. Buyanova, Scopus ID 26536460700.

Websites:
Zavaritsky Institute of Geology and Geochemistry, http://eng.igg.uran.ru;
Ural Federal University, https://urfu.ru/en;
Institute of Metallurgy, http://www.imet-uran.ru.

References

1. Frank M, Smetanin SN, Jelinek M, Vyhlidal D, Kopalkin AA, Shukshin VE, Ivleva LI, Zverev PG, Kubecek V. Synchronously-pumped all-solid-state $SrMoO_4$ Raman laser generating at combined vibrational Raman modes with 26-fold pulse shortening down to 1.4 ps at 1220 nm. Opt Laser Technol. 2019;111:129–133. doi:10.1016/j.optlastec.2018.09.045
2. Künzel R, Umisedo NK, Okuno E, Yoshimura EM, de Azevedo Marques AP. Effects of microwave-assisted hydrothermal treatment and beta particles irradiation on the thermoluminescence and optically stimulated luminescence of $SrMoO_4$ powders. Ceram Int. 2020;46:15018–15026. doi:10.1016/j.ceramint.2020.03.032
3. Yu H, Shi X, Huang L, Kang X, Pan D. Solution-deposited and low temperature-annealed Eu^{3+}/Tb^{3+}-doped $CaMoO_4/SrMoO_4$ luminescent thin films. Lumin J. 2020;225:117371. doi:10.1016/j.jlumin.2020.117371
4. Elakkiya V, Sumathi S. Low-temperature synthesis of environment-friendly cool yellow pigment: Ce substituted $SrMoO_4$. Mater Lett. 2020;263:127246. doi:10.1016/j.matlet.2019.127246
5. Mikhailik VB, Elyashevskyi Yu, Kraus H, Kim HJ, Kapustianyk V, Panasyuk M. Temperature dependence of scintillation properties of $SrMoO_4$. Nucl Instrum Methods Phy Res A. 2015;79:1–5. doi:10.1016/j.nima.2015.04.018

6. Danevich FA. Radiopure tungstate and molybdate crystal scintillators for double beta decay experiments. Int J Mod Phys A. 2017;32(30):1743008. doi:10.1142/S0217751X17430084
7. Guo HH, Zhou D, Pang LX, Qi ZM. Microwave dielectric properties of low firing temperature stable scheelite structured (Ca,Bi)(Mo,V)O_4 solid solution ceramics for LTCC applications. J Eur Ceram. 2019;39:2365–2373. doi:10.1016/j.jeurceramsoc.2019.02.010
8. Yu-Ling Y, Xue-Ming L, Wen-Lin F, Wu-Lin L, Chuan-Yi T. Coprecipitation synthesis and photoluminescence properties of $(Ca_{1-x-y},Ln_y)MoO_4$: xEu^{3+} (Ln = Y, Gd) red phosphors. J Alloys Compd. 2010;505:239–242. doi:10.1016/j.jallcom.2010.06.037
9. Xie A, Yuan X, Wang F, Shi Y, Li J, Liu L, Mu Z. Synthesis and luminescent properties of Eu^{3+}-activated molybdate-based novel red-emitting phosphors for white LEDs. J Alloys Compd. 2010;501:124–129. doi:10.1016/j.jallcom.2010.04.057
10. Zhu Y, Zheng G, Dai Z, Zhang L, Ma Y. Photocatalytic and luminescent properties of $SrMoO_4$ phosphors prepared via hydrothermal method with different stirring speed. J Mater Sci Techno. 2017;33:23–29. doi:10.1016/j.jmst.2016.11.019
11. Guo J, Randall CA, Zhou D, Zhang G, Zhang C, Jin B, Wang H. Correlation between vibrational modes and dielectric properties in $(Ca_{1-3x}Bi_{2x}\Phi_x)MoO_4$ ceramics. J Eur Ceram Soc. 2015;35:4459–2264. doi:10.1016/j.jeurceramsoc.2015.08.020
12. Esaka T. Ionic conduction in substituted scheelite-type oxides. Solid State Ionics. 2000;136:1–9. doi:10.1016/s0167-2738(00)00377-5
13. Cheng J, Liu C, Cao W, Qi M, Shao G. Synthesis and electrical properties of scheelite $Ca_{1-x}Sm_xMoO_{4+\delta}$ solid electrolyte ceramics. Mater Res Bull. 2011;46:185–189. doi:10.1016/j.materresbull.2010.11.019
14. Fansuri H. Catalytic partial oxidation of propylene to acrolein: the catalyst structure, reaction mechanisms and kinetics[dissertation]. Perth (Australia): Curtin University of Technology; 2005. 191 p.
15. Sleight JAW, Aykan K. New nonstoichiometric molybdate, tungstate, and vanadate catalysts with the scheelite-type structure. J Solid State Chem. 1975;13:231–236. doi:10.1016/0022-4596(75)90124-3
16. Guo J, Randall AC, Zhang G, Zhou D, Chen Y, Wang H. Synthesis, structure, and characterization of new low-firing microwave dielectric ceramics: $(Ca_{1-3x}Bi_{2x}\Phi_x)MoO_4$. J Mater Chem C. 2014;2:7364–7372. doi:10.1039/c4tc00698d
17. Mikhaylovskaya ZA, Abrahams I, Petrova SA, Buyanova ES, Tarakina NV, Piankova DV, Morozova MV. Structural, photocatalytic and electroconductive properties of bismuth-substituted $CaMoO_4$. J Sol State Chem. 2020;291:121627. doi:10.1016/j.jssc.2020.121627
18. Mikhaylovskaya ZA, Buyanova ES, Petrova SA, Klimova AV. ABO_4 type scheelite phases in (Ca/Sr)MoO_4 - $BiVO_4$ - $Bi_2Mo_3O_{12}$ systems: synthesis, structure and optical properties. Chimica Techno Acta. 2021;8:20218204. doi:10.15826/chimtech.2021.8.2.04
19. Liang EJ, Huo HL, Wang Z, Chao MJ, Wang JP. Rapid synthesis of $A_2(MoO_4)_3$ (A = Y^{3+} and La^{3+}) with a CO_2 laser. Solid State Sci. 2009;11:139–43. doi:10.1016/j.solidstatesciences.2008.04.008
20. Porotnikova N, Khrustov A, Farlenkov A, Khodimchuk A, Partin G, Animitsa I, Kochetova N, Pavlov D., Ananyev M. Promising $La_2Mo_2O_9$–$La_2Mo_3O_{12}$ composite oxygen-ionic electrolytes: interphase phenomena. ACS Appl Mater Interfaces 2022;14:6180–6193. doi:10.1021/acsami.1c20839
21. Chen Z, Bu W, Zhang N, Shi J. Controlled construction of monodisperse $La_2(MoO_4)_3$:Yb, Tm microarchitectures with upconversion luminescent property. J Phys Chem C. 2008;112:4378–83. doi:10.1021/jp711213r
22. Brazdil JF. Scheelite: a versatile structural template for selective alkene oxidation catalysts. Catal Sci Technol. 2015;5:3452–3458. doi:10.1039/c5cy00387c
23. Antonio MR, Teller RG, Sandstrom DR, Mehicic M, Brazdil JF. Structural characterization of bismuth molybdates by X-ray absorption spectroscopy and powder neutron diffraction profile analysis. J Phys Chem. 1988;92:2939–2944. doi:10.1021/j100321a045
24. Kubelka P, Munk FZ. Ein beitrag zur optik der farbanstriche. Techn Phys. 1931;12:593–601.
25. Shannon RD. Revised effective ionic radii and systematic studies of interatomic distances in halides and chalcogenides. Acta Cryst. A. 1976;32:751–767. doi:10.1107/S0567739476001551
26. Vali R. Electronic properties and phonon spectra of $SrMoO_4$. Comp Mater Sci. 2011;50:2683–2687. doi:10.1016/j.commatsci.2011.04.018
27. Ramarao SD, Roopas Kiran S, Murthy VRK. Structural, lattice vibrational, optical and microwave dielectric studies on $Ca_{1-x}Sr_xMoO_4$ ceramics with scheelite structure. Mater Res Bull. 2014;56:71–79. doi:10.1016/j.materresbull.2014.04.064
28. Porto SPS, Scott JF. Raman Spectra of $CaWO_4$, $SrWO_4$, $CaMoO_4$ and $SrWO_4$. Phys Rev. 1976;157:716–719. doi:10.1103/PHYSREV.157.716
29. Hardcastle FD, Wachs IE. Molecular structure of molybdenum oxide in bismuth molybdates by Raman spectroscopy. J Phys Chem. 1975;95:10763–10772. doi:10.1021/j100179a045
30. Jayaraman A, Wang SY, Shieh SR, Sharma SK, Ming LC. High-pressure Raman study of $SrMoO_4$ up to 37 GPa and pressure-induced phase transitions. J Raman Spectrosc. 1995;26:451–455. doi:10.1002/jrs.1250260609
31. Salje EKH, Carpenter MA, Malcherek T, Boffa Ballaran T. Autocorrelation analysis of infrared spectra from minerals. Eur J Mineral. 2000;12:503–519. doi:10.1127/0935-1221/2000/0012-0503
32. Pankrushina EA, Kobuzov AS, Shchapova YV, Votyakov SL. Analysis of temperature-dependent Raman spectra of minerals: Statistical approaches. J Raman Spectrosc. 2020;51:1549–1562. doi:10.1002/jrs.5825
33. Verma A, Sharma SK. Rare-earth doped/codoped $CaMoO_4$ phosphors: A candidate for solar spectrum conversion. Solid State Sci. 2019;96:105945. doi:10.1016/j.solidstatesciences.2019.105945
34. Zhang Y, Holzwarth NAW, Williams RT. Electronic band structures of the scheelite materials $CaMoO_4$, $CaWO_4$, $PbMoO_4$ and $PbWO_4$. Phys Rev B. 1998;57:12738–12750. doi:10.1103/PhysRevB.57.12738
35. Mikhaylovskaya ZA, Pankrushina EA, Komleva EV, Ushakov AV, Streltsov SV, Abrahams I, Petrova SA. Effect of Bi substitution on the cationic vacancy ordering in $SrMoO_4$-based complex oxides: structure and properties. Mater Sci Eng B. 2022;281:115741. doi:10.1016/j.mseb.2022.115741
36. Maji BK, Jena H, Asuvathraman R, Kutty KVG. Electrical conductivity and thermal expansion behavior of $MMoO_4$ (M = Ca, Sr and Ba). J Alloys Compd. 2015;64:475–479. doi:10.1016/j.jallcom.2015.04.054
37. Irvine JTS, Sinclair DC, West AR. Electroceramics: characterization by impedance spectroscopy. Adv Mat. 1990;2:132–138. doi:10.1002/adma.19900020304
38. Vinke I, Diepgrond J, Boukamp B, de Vries KJ, Burggraaf AJ Bulk and electrochemical properties of $BiVO_4$. Solid State Ionics. 1992;57:83–89. doi:10.1016/0167-2738(92)90067-y
39. Hartmanova M, Le MT, Jergel M, SmatkoV, Kundracik F. Structure and electrical conductivity of multicomponent metal oxides having scheelite structure. Rus J Electrochem. 2009;45:621–629. doi:10.1134/s1023193509060019